M6 ONERA Wing Turbulent Flow Validation, Team 3

Charles Yu, and John Rolfe, and Zerong Huang (Jason)

Purdue University, West Lafayette, IN, 47906, USA

This paper explores the analysis of a computational fluid dynamics (CFD) simulation on the ONERA-M6 wing. The analysis was done using the Ansys Fluent CFD software and uses data from NASA's analysis of the wing in transonic flight conditions, Case 2308 and Case 2565, as a point of comparison. First, the two cases were simulated to validate the CFD model. In addition to these cases, two more flight profiles were analyzed for compressible but non-transonic flight conditions. Comparisons were then drawn between each of the four analyses. The paper covers the setup of the general simulation approach, meshes used, a discussion of each case, and finally draws conclusions across all four simulations.

I. Introduction

The ONERA-M6 wing has long been used in the aerodynamics world to validate CFD models. The original experiment was first conducted in 1972 as a way to study three-dimensional flow properties and results were published. These experiments were conducted at Mach numbers from 0.70 to 0.92 and angles of attack up to 6 degrees. The wing itself is swept, tapered, but without twist and comprised of a single airfoil type across the span. This makes it a realistic yet simple example of three-dimensional transonic flows. The published results of the wind tunnel experiments on the ONERA wing were both of high-quality and accessible to the greater aerodynamic community, ultimately leading to their widespread use for simulation validation.

The simulations discussed in this paper follow two main tests conducted by NASA, Case 2308 and 2565. Case 2308 was a test on the wing at Mach 0.84, a Reynolds number of 14.6e6, and an angle of attack of 3.06 degrees. Case 2565 followed the same Mach and Reynolds number, but increased angle of attack to 6.06 degrees. The Mach number places these cases squarely in a transonic flight profile, which is the primary purpose of the initial studies. These two cases (Case 1 and 2 in this paper) were modeled in Ansys Fluent and validated with test data from NASA. Beyond these two main cases, the team selected two more cases (Case 3 and 4) to act as a point of comparison. These cases matched the Reynolds number and angle of attack of the initial two cases but reduced the Mach number to 0.5 degrees in order to exit the transonic region. The intent of this was to build a baseline for the transonic cases and give context for comparison of flow behavior for each scenario. While there were slight issues with some of the simulations, the results were determined to represent realistic fluid flows. This paper will discuss the specific approach used in each analysis, the meshing and y+ values used, and finally a discussion of the results including comparisons between cases and lessons learned.

II. Approach

The team utilized different grid sizes for the coarse and refined grids in the CFD simulation. Various methods were tested, and the under-relaxation factors were reduced. However, the team was unable to achieve a converged steady-state solution. To assess the quality of the results, residuals, drag coefficients, and lift coefficients were analyzed using iteration plots. Once the best results were obtained, the experimental C_p distribution values from existing data were used as a reference for comparison.

In this section, the approach will be described in detail. The mesh design will be presented, followed by an explanation of the Fluent setup. Additionally, an overview of the residuals and physical quantity plots will be provided. A detailed discussion of residuals and physical quantities for different cases will be included in the results section.

A. Mesh and Grid

The team performed unstructured mesh in all test cases. The coarse grid consists of approximately 6 million nodes, while the medium (refined) grid contains about 9 to 12 million nodes. The mesh is divided into three distinct sections to balance accuracy and computational efficiency. Near the airfoil, an inflation layer is used to capture the boundary layer with high precision, requiring a finer grid due to the sensitivity of this region and its significant impact on the results. The second section is a central box surrounding the area outside the boundary layer but still close to the airfoil, ensuring accurate modeling of flow behavior. The final section covers the remaining flow domain, where a moderately fine grid is sufficient to transmit turbulence model effects to the airfoil while minimizing computational demands. The following Figure 1 shows the refined grid mesh for case 2 in our group.

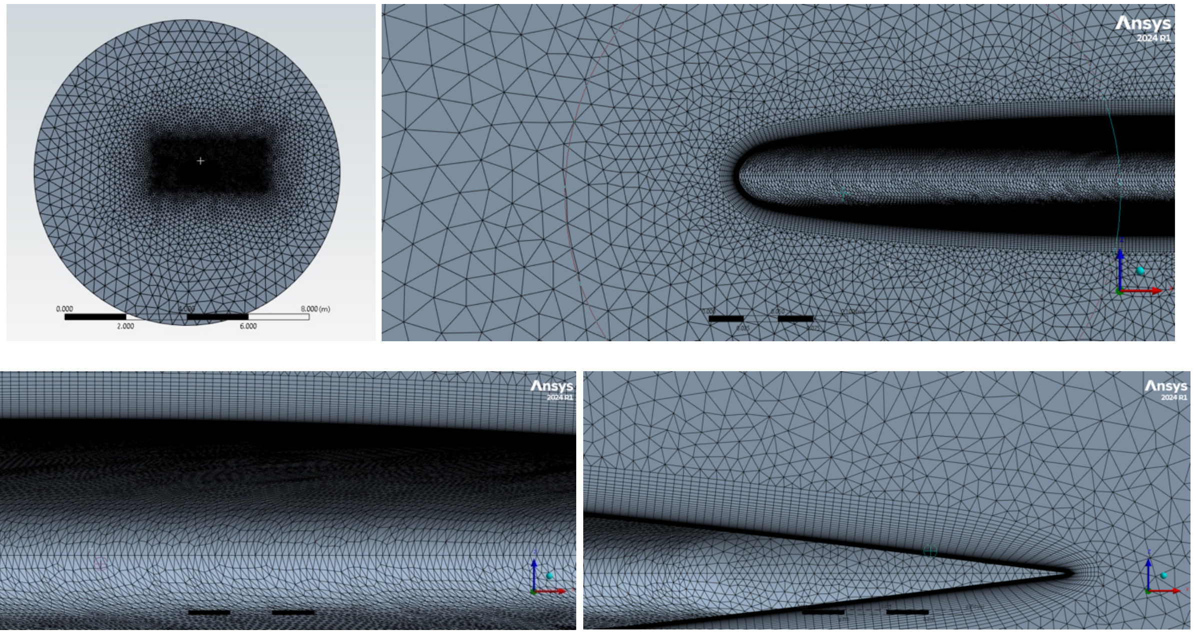

Fig 1. Case 2 Refined Mesh Grid

For each test case, the mesh was adjusted slightly to meet specific requirements. In particular, Case 2 involved expanding the middle concentration area, extending further over the upper surface of the airfoil and beyond the trailing edge. This adjustment was informed by the coarse grid calculation results, which revealed a large shock on the upper wing. To address this, the team increased the concentration area in this region to capture more detailed data and improve accuracy.

The average aspect ratio of the mesh is 284.58, and the maximum skewness is 0.97717. Both values are relatively high, which could potentially impact the results. However, these values represent the best compromise achievable given the computational resources and the use of an unstructured mesh. Table 1 provides detailed information about the mesh for different test cases.

Table 1: Case 2 Refined Mesh Grid

	Case 1	Case 2	Case 3 & Case 4
y plus value	0.8	0.8	0.8
Element size	3.5e-3 m	4e-3 m	3.5e-3 m
Inflation	1.1	1.1	1.125
Nodes	11.151 million	8.425 million	9.060 million
Elements	23.577 million	20.0426 million	19.42 million

The team developed a MATLAB program to calculate the boundary layer thickness of the airfoil, assuming the airfoil behaves as a thin plate. Under the specified Reynolds number, the program estimated the boundary layer thickness to be 0.0123 m. Since the actual boundary layer is expected to be larger, additional inflation layers were added to ensure full coverage of the boundary layer. As shown in Figure 2, the inflation layers effectively capture the boundary layer, as indicated by the scale at the bottom of the figure.

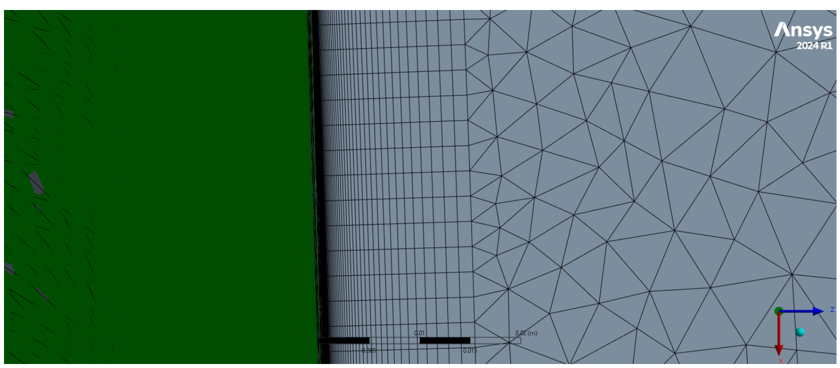

Fig 2. Boundary Layer Prediction

The team established a requirement to maintain a y-plus value of 1 or less to ensure high mesh quality. The thickness of the first layer was calculated based on this y-plus value requirement. To verify compliance, the team analyzed the y-plus value plot to confirm that the mesh met the specified standard. As shown in **Figure 3**, all y-plus values are below 0.75, demonstrating that the mesh satisfies the quality requirement.

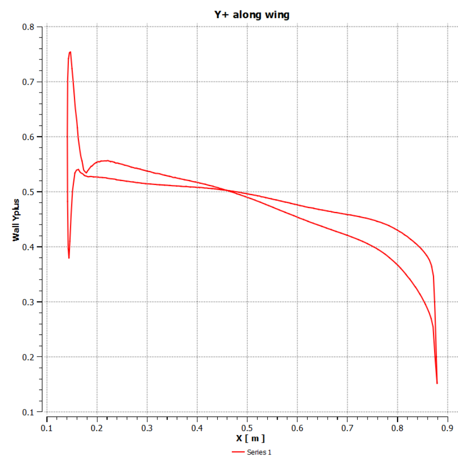

Fig 3. Y Plus Value Verification

B. Fluent Setup

The team input the required air properties and boundary conditions to set up the simulations. However, difficulties arose when selecting the appropriate method to run the simulations. Specifically, the continuity residuals failed to converge to the target value of 10e−6 for steady-state results. In Case 2, the residuals only dropped to 10e−2, while in Case 1, they decreased to 10e−4.

To address this, the team tested the SIMPLEC, SIMPLE, and Coupled methods using the coarse grid to determine which method provided better results while also saving computation time. The results indicated that the Coupled method produced better outcomes for Case 1 and Case 2, whereas the SIMPLEC method performed better in Case 3 and Case 4.

The team also experimented with the first-order upwind scheme to reduce residuals. However, switching back to the second-order upwind scheme caused the residuals to rise again, with no significant improvement observed in subsequent iterations.

C. Residuals and Physical Quantity

The quality of the results can be evaluated using the residuals and the plots of physical quantities versus iterations. Residuals converging to less than 10e-6 indicate a steady-state solution. However, in Case 2, which involves a higher angle of attack and transonic conditions, a large shock on the upper surface of the airfoil causes the continuity residuals to struggle to converge to small values. In contrast, Case 1, which features a lower angle of attack, experiences a smaller shock, allowing the continuity residuals to perform better and converge to a smaller value compared to the 6.06-degree angle of attack in Case 2.

The team monitored the lift coefficient and drag coefficient as key physical quantities to assess result quality. A good solution is characterized by smooth and stable lift and drag coefficient curves, whereas fluctuating and unstable curves indicate poor quality. By adjusting the simulation methods, the team was able to achieve smooth lift and drag coefficient curves, ensuring reliable results. Further details on these results will be provided in the results section for each case.

III. Results

A. Case 1

Case 1 analyzed the ONERA M6 wing at a speed of Mach 0.84 at 3.06 degrees AoA. For this case, attached flow with a developing shock region was the anticipated result. This case was evaluated for 1,000 and 1,500 iterations for the coarse and refined grids, respectively, using the SIMPLE solver with the Spalart-Allmaras turbulence model. Residual convergence was set at 1e-6 with continuity being set at 1e-4.

Both grids converged within 200 iterations to their final solutions; small oscillations were present in the residual plots shown in Figure 4, but these were deemed acceptable as the magnitude of these oscillations was less than 1e-5 and would have little overall impact on the solution. It is possible that additional iterations would eventually result in a fully converged solution; however, doing so would have needlessly extended the computational time required without significantly affecting the results.

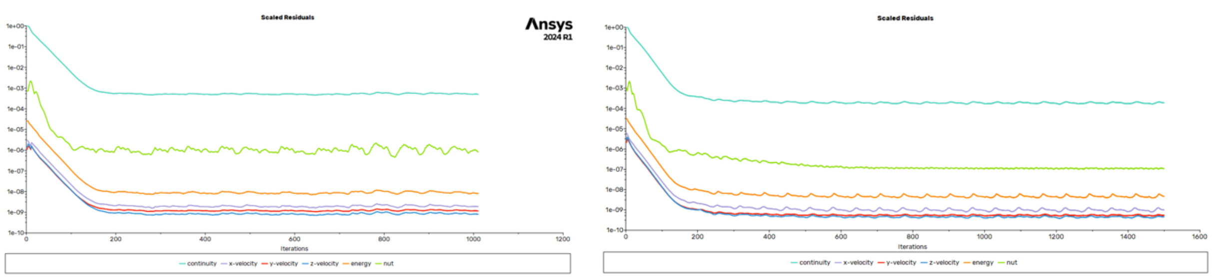

Figure 4: Case 1 residual plots for coarse (left) and refined (right) meshes

For both meshes, lift and drag coefficients were extracted from the simulation results and are shown in Figures 5 and 6, respectively. These values align very well with each other; the coarse mesh returned lift and drag coefficients of 0.26253 and 0.01847, respectively, while the refined mesh returned these coefficients as 0.026251 and 0.01852. These values match with an error of less than 0.5% for the drag coefficient and 0.01% for the lift coefficient; this indicates that the solution is grid independent and performing additional refinements to the mesh will not cause a significant change in the converged values.

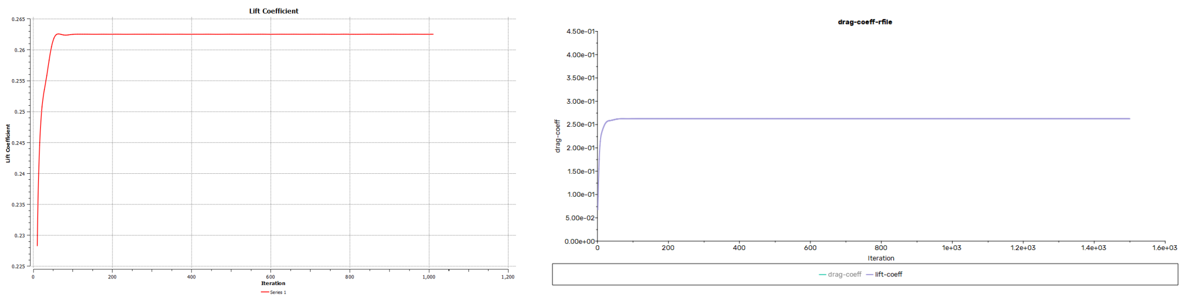

Figure 5: Lift coefficient progression for coarse (left) and refined (right) meshes

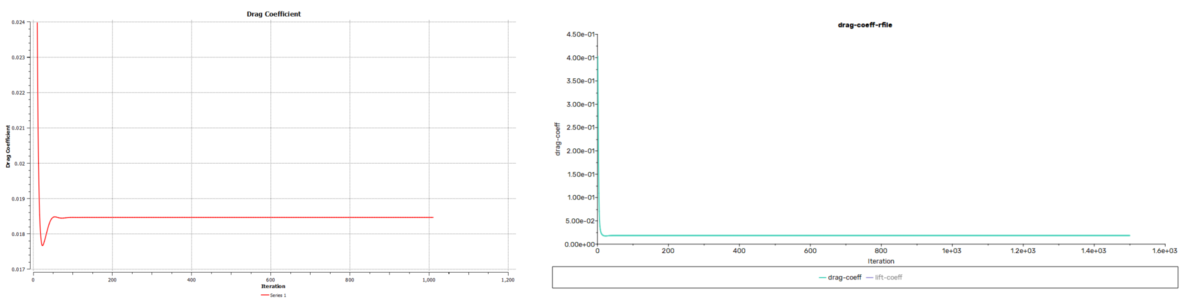

Figure 6: Drag coefficient progression for coarse (left) and refined (right) meshes

Additionally, for the refined mesh, the pressure distribution over the wing's surface was obtained as the flight conditions fall within the transonic range. This, combined with the rear-swept design of the wing, makes it highly likely that there will be a local shock forming over the upper surface of the wing. The calculated pressure distribution, shown in Figure 7, confirms this prediction. The local shock, characterized by the low (blue) pressure gradients, begins near the wing root and grows along the wing's semispan. Interestingly, at the leading-edge wingtip, there is a small region of low pressure versus the high-pressure concentration on the rest of the leading-edge; this can be explained by the presence of flow turning over the lower surface into a wingtip vortex; streamlines plotted over the wingtip shown in Figure 8 confirms this behavior.

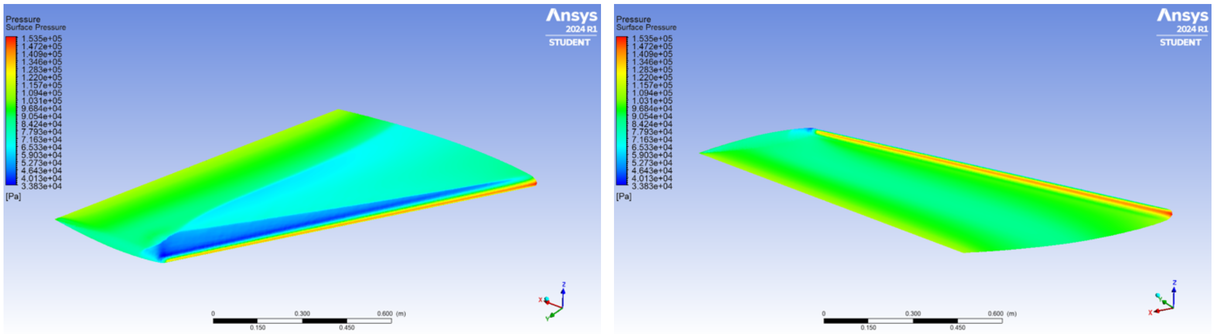

Figure 7: Pressure distribution over the upper (left) and lower (right) surfaces of the wing.

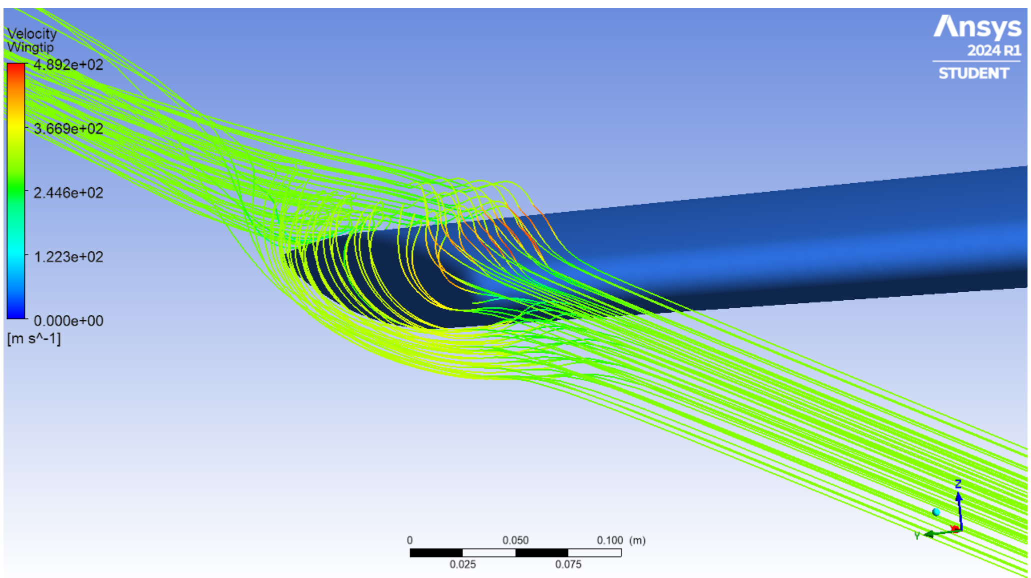

Figure 8: Wingtip vortex causing low pressure over the leading-edge wingtip.

We were interested in examining the evolution of this low-pressure front moving across the wing, so three semispan percentages were chosen as reference points where we would capture various parameters. The chosen positions were at 20%, 65%, and 96% of the overall semispan; this allowed us to approximate root, mid-span, and wingtip positions. More importantly, these positions align with the measurement positions of the papers provided to us as reference (Gleize et. Al, 2015), so this allowed us to compare the accuracy of our results with published data.

The first set of measurements collected at these wing positions was the pressure and velocity gradients in the airflow, shown in Table 2. The pressure and velocity deviations are, expectedly, mirror images of each other as higher velocities will result in lower airstream pressure; additionally, as the reference point moves further along the wing's span, the size of this disturbance area increases which is expected due to the wing sweep causing spanwise flow to increase the airflow disturbance away from the wing root. Case 2, detailed below, shows how these disturbances transition into stall conditions as the angle of attack continues to increase.

Table 2: Pressure and Velocity gradients at different wing positions

	20% semispan	65% semispan	96% semispan
Pressure	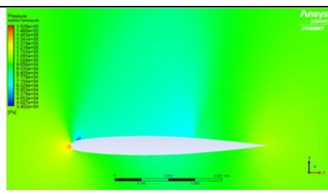	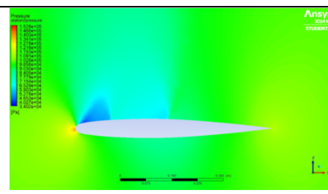	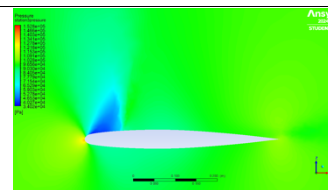
Velocity	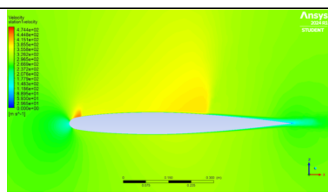	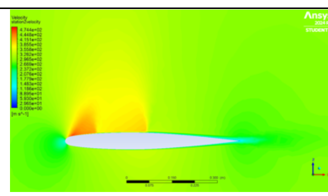	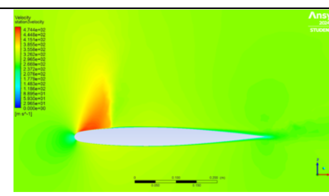

The second set of measurements we collected was the pressure distribution along the airfoil. This provided us with the best method to determine the accuracy of our simulations as the reference papers contained pressure distribution plots we could use as a comparison. The pressure from the simulation results compared with those from published data is shown in Table 3. Here, the values obtained from our simulations agrees with published data; the maximum pressure coefficient has approximately the same value as the reference data, and the positions of the pressure increases follow the same spanwise evolution as is described by the reference data.

Table 3: Pressure coefficient plots at different wing positions

	20% semispan	65% semispan	96% semispan
Simulated	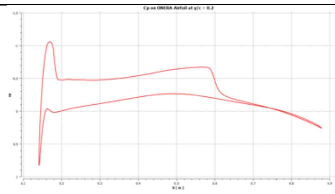	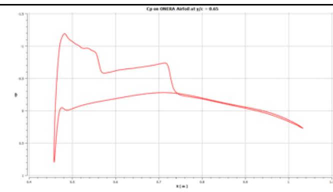	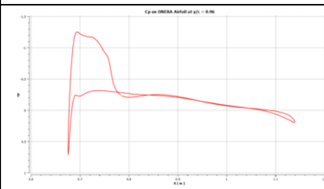
Reference (Gleize et. al, 2015)	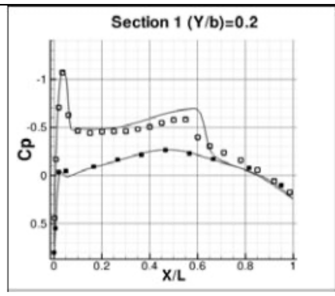	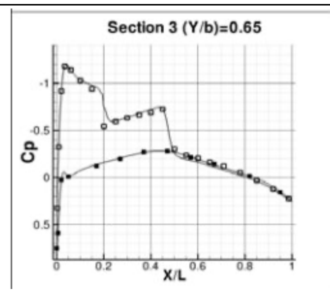	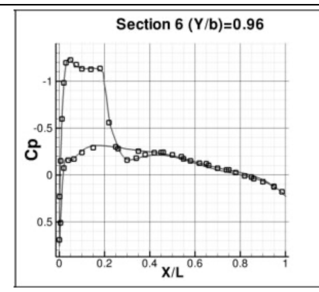

Finally, we examined the wall shear stress at these three locations. Given the results from this simulation, we expected to see sharp drops in the shear stress corresponding to the locations where the pressure coefficient changes; as seen in Table 4, these drops do occur as predicted. The locations of the shear stress drops coincide with the increases in the pressure coefficient and, if they were overlaid on the wing, would match with the various changes in pressure and velocity. Additionally, the maximum shear stress increases as measurements are taken further out on the semispan; the wing root has a maximum shear stress of approximately 292 Pa while the wingtip has a maximum shear stress of approximately 325 Pa; this aligns with the increase in spanwise flow from the root to the wingtip. One observation to note is the sharp drop in shear stress at the wingtip (96% semispan) to about 20 Pa; this indicates that flow separation, which would occur if the shear stress reached zero, is close to happening at this location.

Table 4: Wall shear stress plots at different wing positions

20% semispan	65% semispan	96% semispan
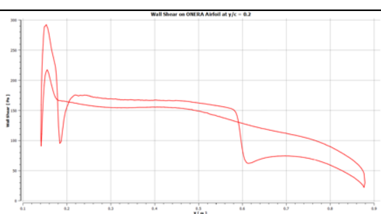	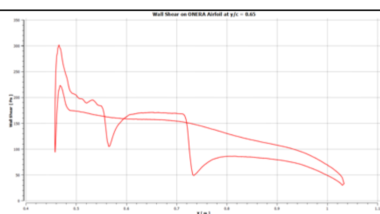	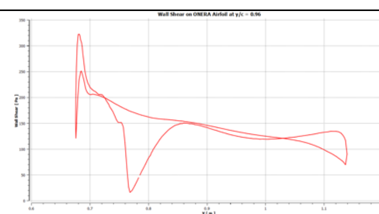

B. Case 2

Case 2 analyzed the ONERA M6 wing at a Mach number of 0.84 and an angle of attack of 6.06 degrees. For this case, an attached flow with the development of a strong shock region was anticipated. The simulations were conducted for 520 iterations on the coarse grid and 800 iterations on the refined grid, using the Coupled method with the Spalart-Allmaras turbulence model. A residual convergence target of 10e−6 was set, but the continuity residuals only converged to 10e−2. The residuals serve as indicators of the calculation and iteration quality.

The team performed simulations on both the coarse and refined grids, with the refined grid providing slightly better results. **Figure 9** illustrates the differences in residual convergence between the coarse and refined grids, highlighting the improved accuracy achieved with the refined grid.

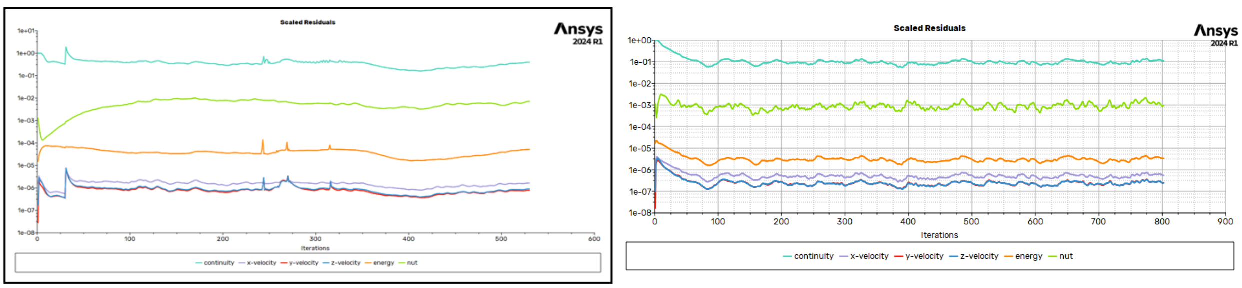

Figure 9: Residuals Comparison Between Coarse Grid (Left) and Refined Grid (Right).

The residuals in the refined grid calculation are smoother and do not exhibit any spikes, indicating better numerical stability and convergence. Similarly, the physical properties, such as the lift and drag coefficients, demonstrate a consistent and smooth behavior compared to the coarse grid results. Figure 10 and Figure 11 present a comparison of the residuals and physical property trends, respectively, highlighting the improved performance of the refined grid.

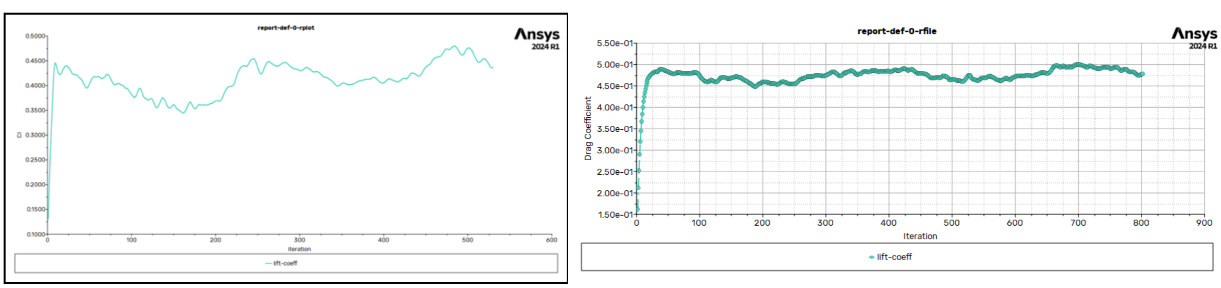

Figure 10: Lift Coefficient Comparison Between Coarse Grid (Left) and Refined Grid (Right).

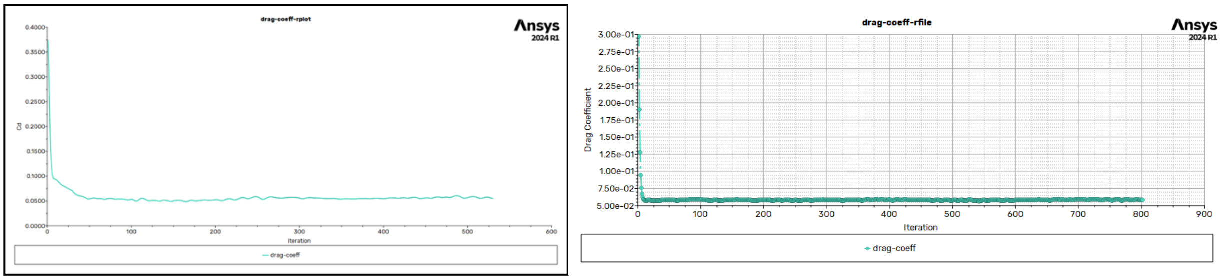

Figure 11: Drag Coefficient Comparison Between Coarse Grid (Left) and Refined Grid (Right).

Both the lift and drag coefficient residual plots become smoother and more stable with the refined mesh, demonstrating that the increased number of nodes and elements contributes to improved result quality. However, despite the improvements, the lift coefficient does not fully converge to a steady-state result, indicating that a true steady state was not achieved. The final calculated lift coefficient for the wing is 0.4783, while the drag coefficient is 0.0584.

After analyzing the quality of the result, the team performed the analysis on coefficient of pressure (C_p) distribution on the wing. The following Figure 12 is the C_p contour plot on the upper surface of the wing.

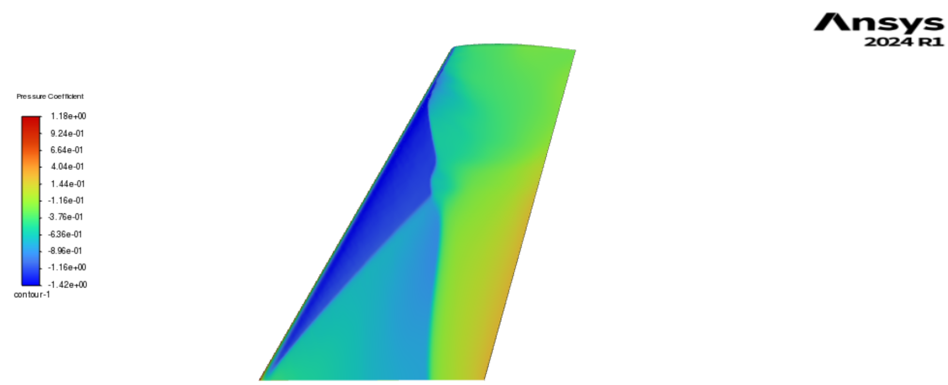

Figure 12: Pressure Coefficient Contour on Upper Surface.

The pressure contour reveals two distinct pressure increases: one near the leading edge and another at the middle of the wing. These sudden pressure rises indicate the presence of shocks on the upper surface of the wing, caused by the transonic flow conditions. At the wingtip, the shock is confined to the leading edge. To further investigate and analyze the shock behavior, the team focused on three specific sections along the wingspan: 20%, 65%, and 96%. The shock characteristics at these sections are illustrated in Figure 13 and Figure 14, highlighting the variations in shock behavior across the wing.

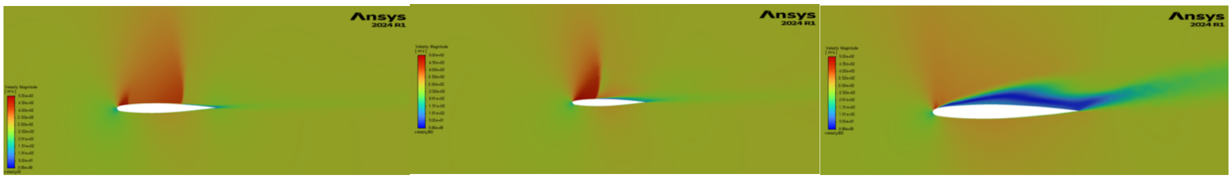

Figure 13: Velocity Contour on Wingspan: 20% (left) 65% (middle) 96% (right).

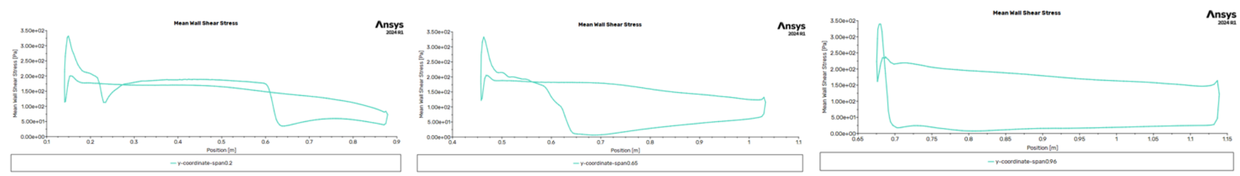

Figure 14: Shear Stress on Wingspan: 20% (left) 65% (middle) 96% (right).

The velocity contours demonstrate trends similar to the C_p contours, with velocity decreasing as pressure increases. At the wing root, the shock appears near the trailing edge, and closer inspection of the graph reveals a stronger shock near the leading edge. At the middle of the wing, the shock is located near the center of the wing chord, while at the wingtip, the shock is weaker, situated at the leading edge, with flow separation observed on the wing.

The shear stress plots further confirm these findings, showing a sudden drop in shear stress where shocks occur. This behavior is consistent with the presence of shocks. At the wing root, the two shocks are particularly evident in the first shear stress plot, providing a clearer view of the flow behavior.

Finally, the team compared the C_p values obtained from the simulation with experimental data published on the NASA website [2]. The comparisons were made at 20%, 65%, and 96% of the wingspan, corresponding to sections 1, 3, and 6 from the NASA data. Figure 15 presents the experimental data alongside the simulation results, plotted together for comparison.

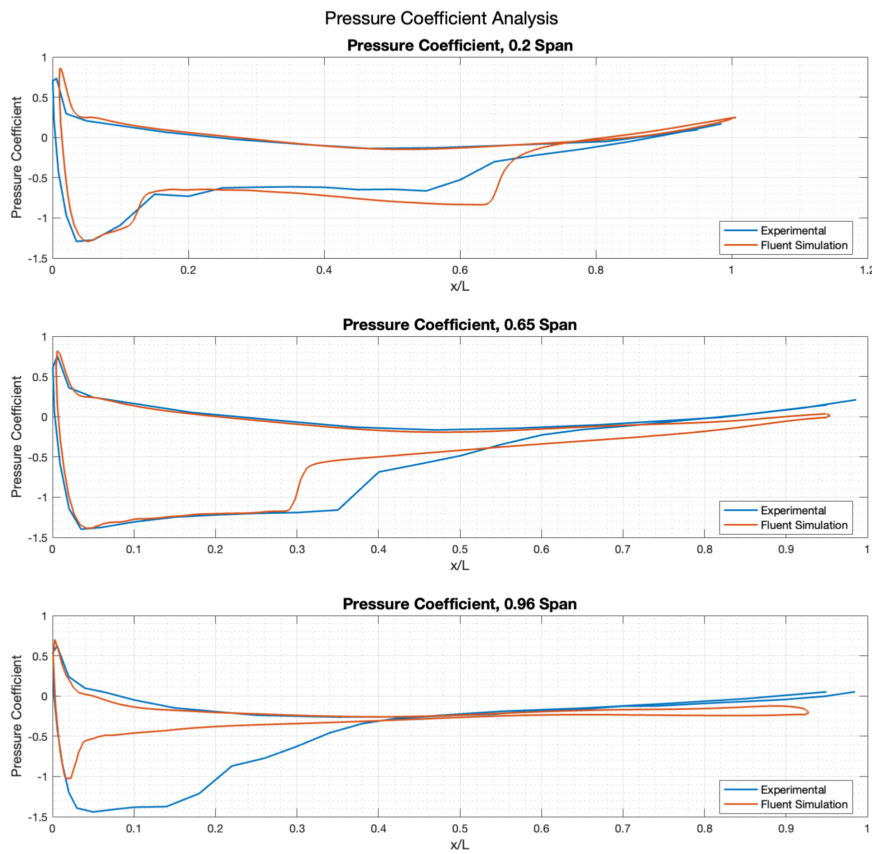

Figure 15: Cp comparison between the Experimental and Simulation

The results show similar shapes and trends to the experimental data; however, as the analysis approaches the wingtip, the results become less coherent. This discrepancy can be attributed to several factors. First, the mesh resolution near the wingtip is not fine enough to capture the complex flow dynamics accurately. To address this, implementing a structured mesh in future simulations could be beneficial, as it would reduce the occurrence of high aspect ratios and skewness that can degrade the solution quality. Additionally, refining the mesh specifically in critical areas, such as near the wingtip and shock regions, could improve the accuracy of the results. Second, the turbulence model used in this simulation does not precisely replicate the flow conditions present in the wind tunnel experiments. Exploring alternative turbulence models or hybrid methods might provide better alignment with experimental data. Third, the iteration time and solution method employed in this study could be optimized. For instance, conducting additional iterations or using advanced convergence techniques might yield more reliable and stable results.

In conclusion, while Case 2 demonstrated the expected flow behavior, including the development of a strong shock on the upper surface, there remains significant room for improvement. By addressing mesh quality, turbulence modeling, and simulation methods, future work could achieve greater accuracy and consistency across all regions of the wing. These refinements would provide a more robust comparison with experimental data and a deeper understanding of the aerodynamic behavior under transonic conditions.

C. Case 3

Case 3 runs the ONERA-M6 wing at a 3.06-degree angle of attack and a Mach number of 0.5. The purpose of this experiment is to contrast how the wing behaves outside of the transonic region. The angle of attack is chosen to allow for direct comparison to Case 1, and 0.5 was chosen as the Mach number such that shocks will not form, but compressible effects will still act on the wing. In addition to these initial choices, Reynolds number was maintained at 14.6e6 to best isolate the change in Mach numbers specifically without generating secondary effects. To set these properties, temperature and geometric properties were fixed, viscosity was calculated using the Sutherland assumption, and finally density was calculated to meet the Reynolds number target. This led to different boundary layer and y+ results and a new mesh was generated for this case to ensure the same grid fidelity was achieved even with the changing properties. This setup is discussed more in the approach section.

The Case 3 analysis was run to 1500 iterations using the SIMPLE solver and a Spalart-Allmaras turbulence model. Residuals were set to their recommended values of 1e-6 with one exception of continuity being set at 1e-4. These values were chosen based on experience with previous calculations completed throughout the class and based on observations of the convergence process. Both a coarse mesh and medium mesh were used in this process, each converging to reasonable outcomes

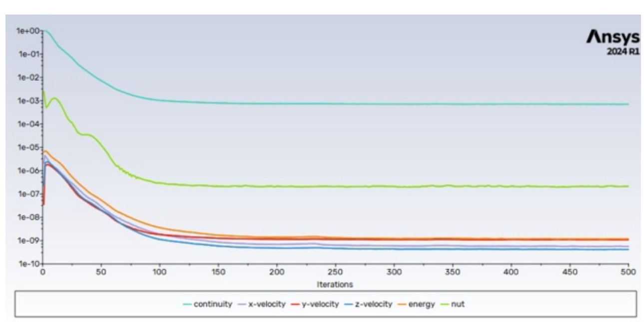

Fig 16: Coarse Mesh Residuals

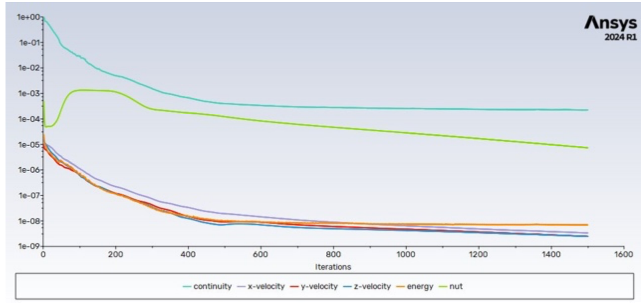

Fig 16: Medium Mesh Residuals

As seen in Figure 15 and 16, energy, x, y, and z velocity all converge quickly to within the specified tolerance, however for the coarse grid continuity does not fully meet the tolerances and neither nut nor continuity meet their tolerance limits in the refined mesh. This can be expected for continuity given that it is typically the last to converge, and in the case of the refined mesh, nut residuals are in the process of decreasing. If more iterations were used, it is likely that these residuals would fully converge, however given the project time constraints and relatively accurate outcomes, this was not attempted.

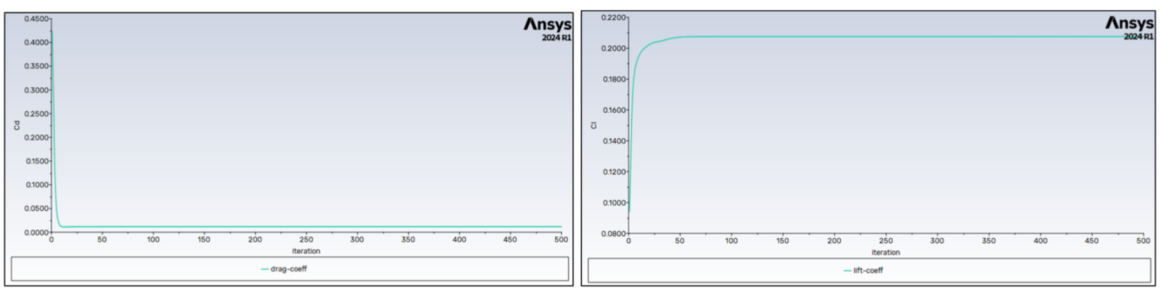

Fig 17. Coarse Mesh Coefficient of Lift and Drag

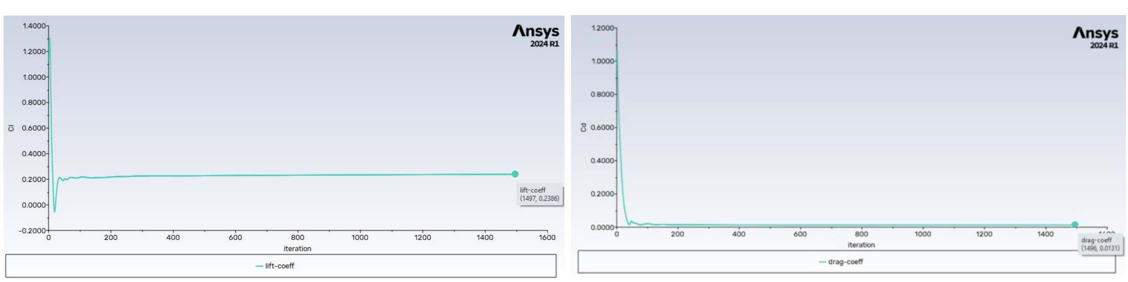

Fig 18. Medium Mesh Coefficient of Lift and Drag

Figure 17 and 18 show lift and drag coefficients for the two grid refinements. For the coarse grid, $C_l = 0.207$ and $C_d = 0.0117$, and for the medium grid $C_l = 0.239$ and $C_d = 0.0131$. This validates the solution as the change in results from the different grid refinements is relatively small. Similarly, there are no meaningful changes in coefficients beyond 75 iterations for the coarse grid and 150 iterations for the medium grid. This provides a second assurance that the residuals not fully converging does not affect the solutions in a meaningful way since increasing the number of iterations would not change the coefficients as long as there is no dramatic deviation from the existing trends.

With the simulation complete, certain sections along the wingspan were analyzed and compared against Case 1 or the recorded wind tunnel testing. The specific sections were chosen to match the location of data recorded in wind tunnel experiments such that Case 1 and 2 could be validated. Pressure and velocity profiles were the primary points of analysis, but shear stress and pressure coefficient on the surface of the wing were also measured.

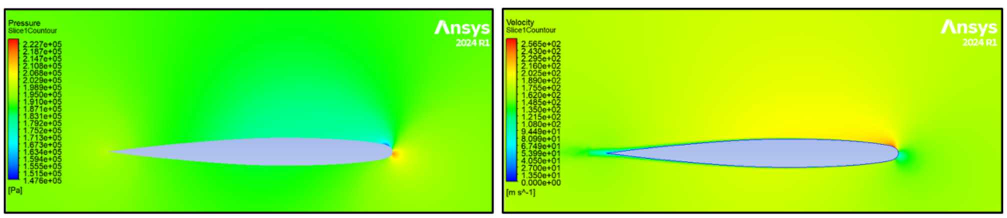

Fig 19. Pressure(left) and Velocity(right) Contours at y/b = 0.20

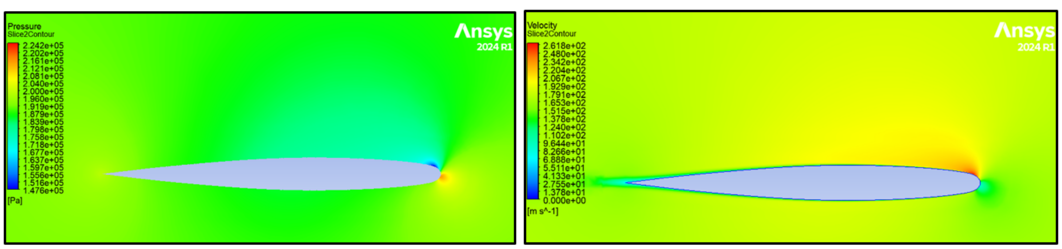

Fig 20. Pressure(left) and Velocity(right) Contours at y/b = 0.65

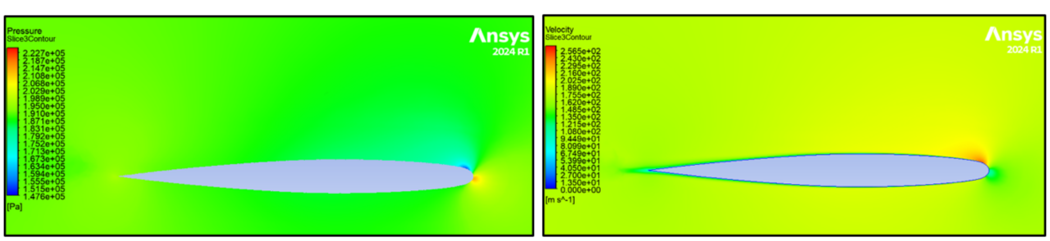

Fig 21. Pressure(left) and Velocity(right) Contours at y/b = 0.96

The pressure and velocity contours show very similar results as they are inversely related by Bernoulli's principle. There are certain properties of the flow that are worth noting. First, one can see the low pressure/ high velocity on the upper surface of the airfoils at each section on the wing. Notably, there are no pressure waves formed by shocks as seen in the first two cases. In addition to this, the leading-edge stagnation point is clearly seen as a point of highest pressure/ zero velocity. The flow exiting the trailing-edge of the airfoil can also be best shown as a low-speed flow caused by the boundary layers merging to meet the Kutta condition. There is very little change in pressure profile across the different wing sections, however it is interesting to note that the difference in pressure, particularly near the leading edge, is greatest for y/b = 0.65. While it is not immediately clear what is causing this section of the wing the experience the greatest pressure differential, it could potentially be a combination of the effects from sweeping the wing and interaction with the wingtip vortex generating a sort of local maximum flow velocity.

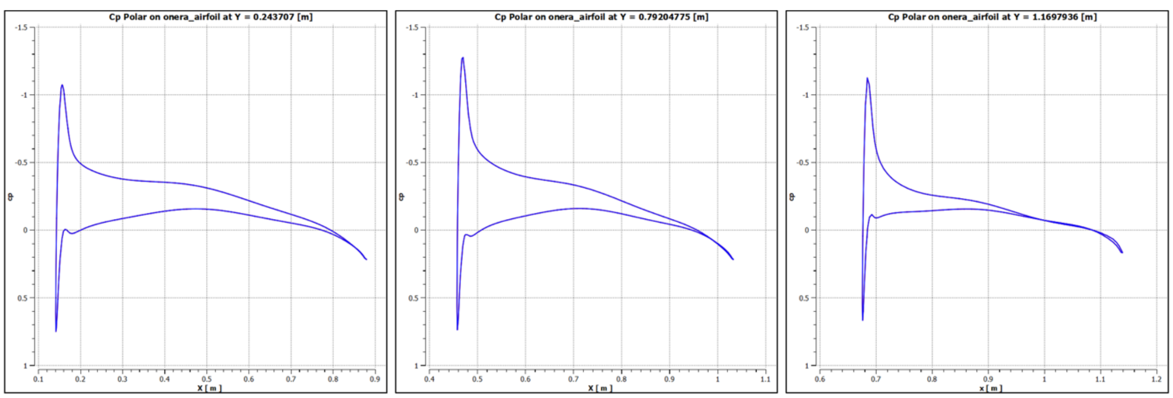

Fig 21. C_p along Chord at y/b = 0.20, 0.65, and 0.95 respectively

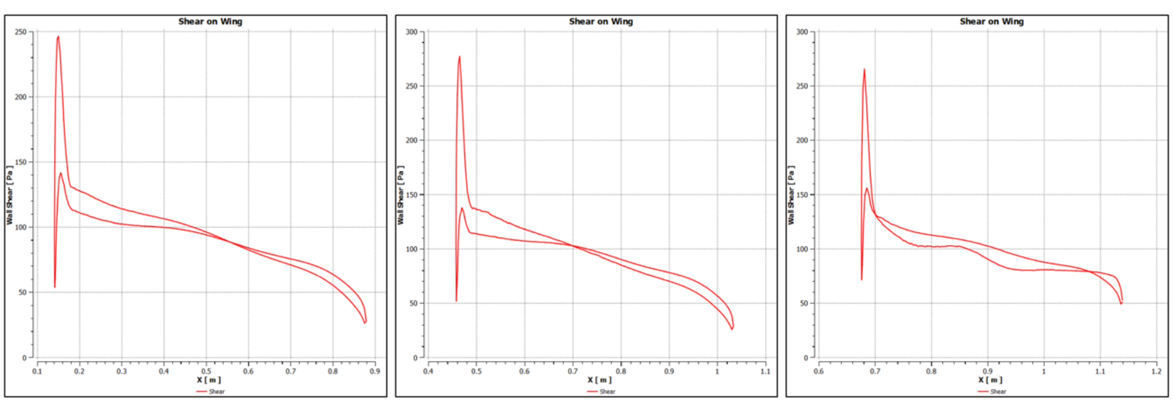

Fig 22. Shear Stress along Chord at y/b = 0.20, 0.65, and 0.95 respectively

Similarly, Figures 21 and 22 show the coefficient of pressure and shear respectively along the cross-section at different span locations. The coefficient of pressure plots in Figure 21 more clearly illustrates 3D wing effects as it shows a greater pressure difference between the upper and lower surfaces for the sections closer to the wing root than the wing tip. Finally, the shear plots follow a relatively predictable pattern along the chord, with increases in shear forces corresponding to the locations of greater pressure. The main spike in shear at the leading edge clearly corresponds with the area just past the stagnation point where pressures are greatest. This also accounts for the wing effects discussed earlier with shear stress acting most significantly on the root section and tapering off slightly by the wing tip.

Ultimately these plots help determine that the ONERA-M6 wing behaves relatively normally at 3.06 degrees angle of attack in sub-transonic flight. The pressure contours show how the flow moves around the wing at the 3.06-degree angle of attack condition, far from stall, and these visuals are supported numerically with the chord-wise shear and C_p plots. When compared to its counterpart, Case 1, Case 3 displays similar patterns without the shocks forming on the upper surface of the wing. Lift and drag appear relatively similar, however there are reductions in both lift and drag which is predicted from the lack of shocks. Similarly, the lift to drag ratio increases in Case 3 relative to Case 1, which matches with the expected behavior of shocks decreasing efficiency. With the fidelity granted from the refined mesh and a reasonable convergence of residuals, this solution accurately displays predicted flow patterns.

D. Case 4

Case 4 was selected to explore flow at slower velocities than the transonic region in order to contrast with Case 2. To do this, the Mach number was chosen as 0.5 because it is far from transonic, and the angle of attack was chosen to be 6.06 degrees in order to directly compare to Case 2. As with Case 3, the temperature was fixed, the Sutherland approximation was used for viscosity, and density was determined such that Reynolds number was 14.6e6 for flow similarity between all cases. The same mesh was used for Case 3 and 4 since the flow conditions were the same, and therefore y+ would be approximately the same. Additionally, the same solver methods of SIMPLE and Spalart-Allmaras were used for simplicity. This allowed for a straightforward setup, while maintaining the level of accuracy expected from a refined, medium grid solution.

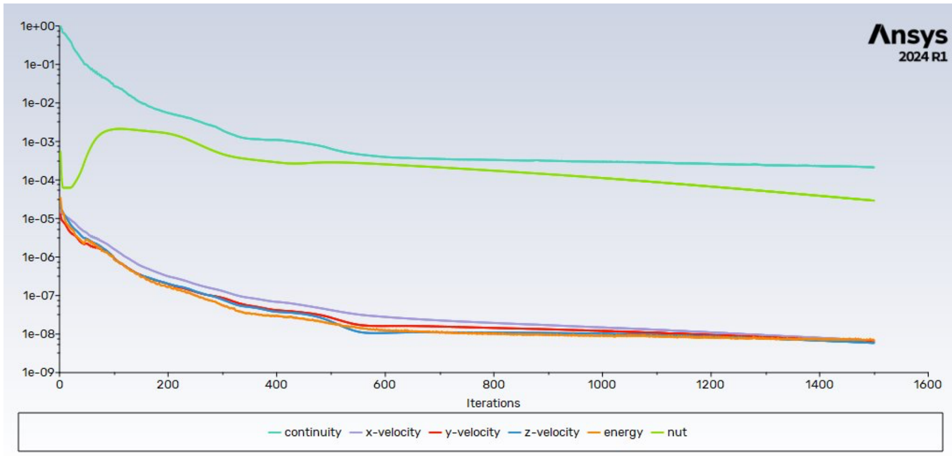

Fig 22. Case 4 Residuals

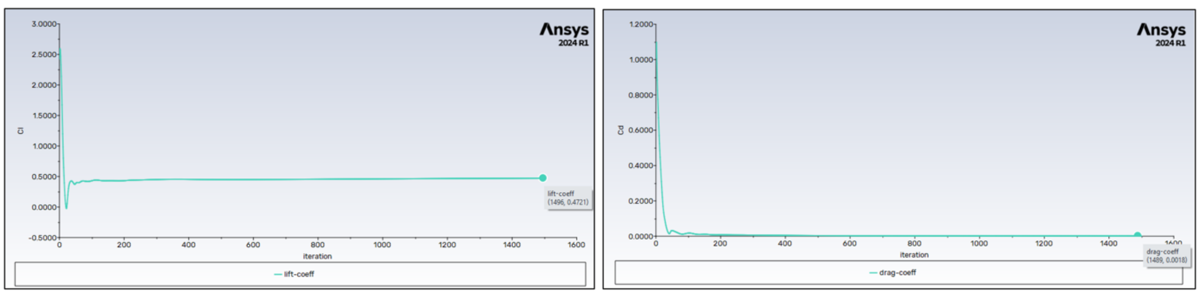

Fig 23. Case 4 C_l and C_d Convergence

Considering the residuals shown in Figure 22, Case 4 converged in energy, x, y, and z velocity. Similarly to Case 3, nut and continuity did not fully meet their tolerance requirements of 1e-6 and 1e-4 respectively. The simulation ended after 1500 iterations, however given the trajectory of the residual plots, it is likely that more iterations would eventually reduce the residual within tolerances. This could not be done within the time allotted for the project as discussed in Case 3 due to the availability of computers and time constraints, however the residuals were reduced to a level that produces consistent results. The coefficient of lift and drag are shown in Figure 23, and display convergence to a single value within 200 iterations. There is no oscillation or divergence after this point, which lends credibility to the accuracy of the solutions. It is for these reasons that this solution was accepted, and more iterations are not required.

After converging, Case 4 displays a lift coefficient of 0.4722 and drag coefficient of 0.0017783, seen in **Figure 23**. The lift coefficient in this case makes sense and is predictable for the wing, validated because both angle of attack and lift are approximately twice that of Case 3, in alignment with common airfoil theories. On the other hand, the drag coefficient is suspiciously low. It does not make sense that drag would be on the order of 10-3 while drag in the previous 3 cases were on the order of 10-2. Similarly, any common wing design should not decrease in drag for an increase in angle of attack if starting from a positive angle of attack. This error in drag is likely not caused by the methods used since the residuals plot and coefficient of lift match expectations, however it is possible that one of the input parameters or reference values was given incorrectly, leading to this error in results.

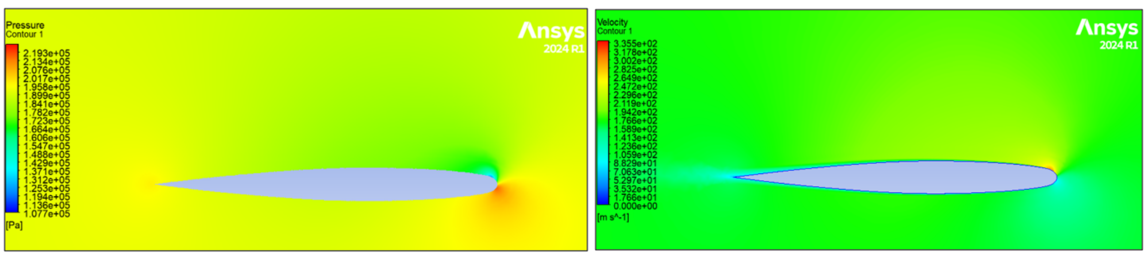

Fig 24. Pressure(left) and Velocity(right) Contours at y/b = 0.20

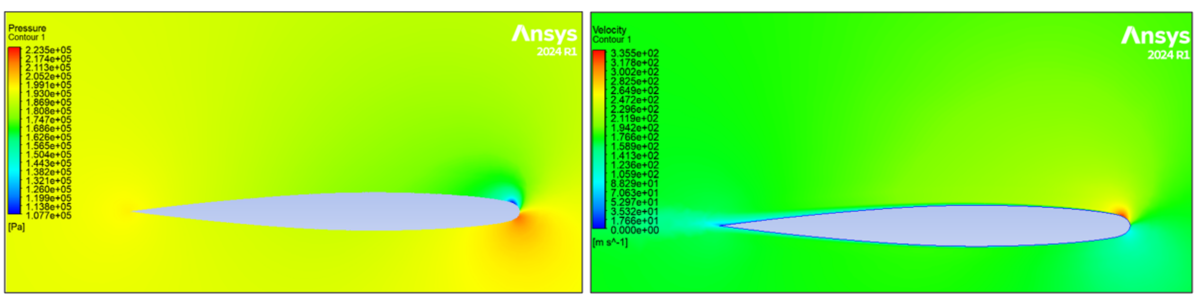

Fig 25. Pressure(left) and Velocity(right) Contours at y/b = 0.65

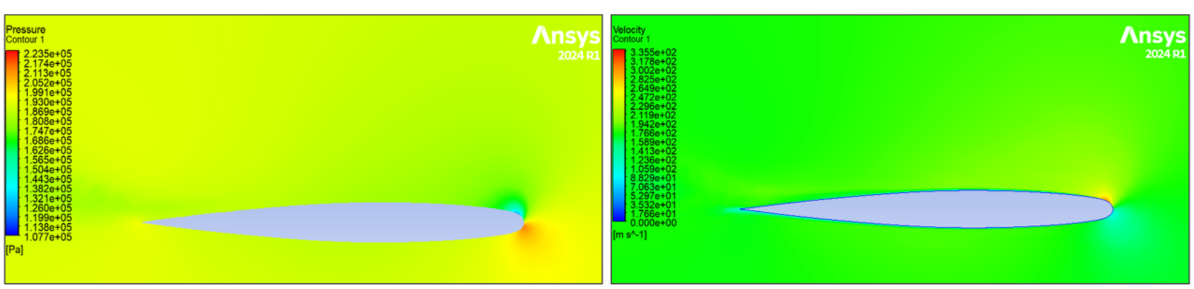

Fig 26. Pressure(left) and Velocity(right) Contours at y/b = 0.96

Figures 24, 25, and 26 display the pressure and relative fluid velocity on the airfoil. As discussed in Case 3, pressure and velocity are inversely related, so the contour plots reflect one another. While the local velocity at certain points on the airfoil is greater in the 6.06-degree angle of attack condition, particularly on the upper surface directly behind the leading edge, there are no shocks forming. This is expected behavior for the Mach 0.5 flow condition. Additionally, the same predicted behaviors occur in Case 4 as Case 3 such as low pressure (high velocity) upper surface, and high pressure (low velocity) on the leading edge and lower surface. The leading-edge stagnation point can be seen clearly as high pressure on the leading edge of each section. This stagnation point is clearly shifted downwards as compared to the 3.06-degree angle of attack case, which matches the increase flow approach angle of Case 4. Next, the boundary layer exiting the trailing-edge of the airfoil is visible as relative high pressure or low velocity in Figure 24 and 25. At the wingtip section, Figure 26, the wing tip vortex can be seen as a low-pressure zone aft and slightly above the chord line of the airfoil. The three figures also show the same 3D effects as in Case 3 with the wing tip section displaying the least pressure differential. Additionally, the same behavior of the middle wing section displaying the greatest difference in high and low pressure can be seen. It is most visible when comparing the low-pressure bubble on the upper surface near the leading edge in **Figure 25** as compared to the other two wing cross-sections. As with Case 3, this is likely the result of interaction between the wingtip vortex and swept wing generating faster local flow, but a more comprehensive simulation would be required to prove this.

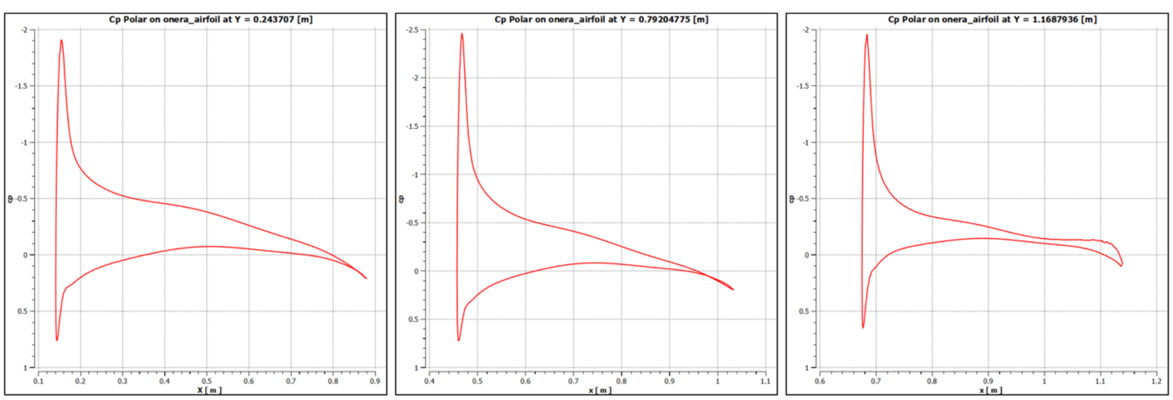

Fig 27. C_p along Chord at y/b = 0.20, 0.65, and 0.95 respectively

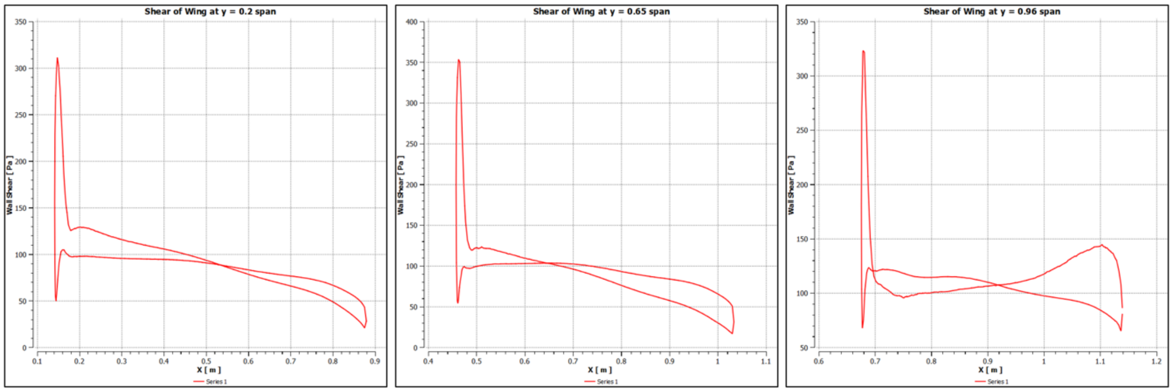

Fig 28. Shear Stress along Chord at y/b = 0.20, 0.65, and 0.95 respectively

The coefficient of pressure and shear stress graphs show the force distributions at the analyzed wing cross-sections. These plots closely resemble their Case 3 counterparts with a few notable features. First, the C_p plot displays a slightly larger difference in pressure between upper and lower surfaces than in Case 3, which is expected due to the higher angle of attack. Similarly, observations of 3D effects on the wing made using the pressure contours can be validated by comparing the reduction in C_p differential between surfaces at the wing tip. The specific pressure distribution can also be used to validate the observation that there is no shock on the wing given that the pressure coefficient has none of the discontinuities or extreme gradients representative of a shock. In addition, the shear stress plots are similar to Case 3, following the intuitive trend of higher shear at locations of higher pressure. One unique behavior shown here is an increase in shear stress near the wing tip's trailing-edge. This shear increase in Figure 28 is matched by a pressure increase in Figure 27, which could be caused by a larger wing tip vortex due to angle of attack. Finally, it is interesting that the magnitude of the shear stress is like that of Case 3 given that drag coefficient is an order of magnitude less. This would indicate that the flow physics simulation in Case 4 is similar to Case 3, but the process of reporting the drag coefficient generated and error leading to the discrepancy.

When looking at Case 2, the transonic counterpart to Case 4, there is a notable lack of shocks across the wing. The lift coefficient is slightly higher than that of Case 2, which is inverse of the relationship between Case 1 and 3. One possible explanation of this behavior is the location of the shocks. Case 1 shows shocks further back on the airfoil, leading to a larger low-pressure zone. Case 2 generated shocks near the leading edge, reducing the area of wing experiencing high-speed, low-pressure flow. This may explain why Case 3 generates less lift than Case 1, but Case 4 generates more lift than Case 2. While it is not reasonable to compare drag for Case 4 given the know issue in calculations, a theoretical reassessment should show that Case 4 will have relatively less drag than Case 2 as wave drag would not occur. In total, Case 4 shows typical pressure and shear properties across its span, in direct contrast to the shocks of Case 2.

IV. Conclusion

In this project, our team examined the performance of the ONERA M6 wing across several different flow conditions to examine how these variations affected the wing's performance. The flow conditions we examined covered high subsonic and transonic flight speeds – Mach 0.5 and 0.84, respectively – at mild to medium angles of attack – 3.06 and 6.06 degrees, respectively. To accomplish this, two refinement levels of meshes were simulated using appropriate solver methods to obtain nearly converged results; due to the unsteady, transonic nature in two of our cases, an exact converged solution was not obtainable, but the oscillations present did not have a noticeable effect on the numerical results across their cycle. The high subsonic flow cases converged more quickly and stably to a solution, but in all cases, the continuity and nut residuals remained above the ideal 1e-6 criteria that was used for the velocity residuals. After completing the simulations, we analyzed the lift and drag coefficients of each case, the pressure gradients over the entire wing, and the pressure gradients, velocity gradients, pressure coefficients, and shear stresses at various span locations. From this information, we concluded that, for Mach 0.84 at 3 degrees angle of attack, the ONERA M6 wing displays attached flow with local supersonic conditions; increasing the angle of attack to 6 degrees expectedly increases the lift coefficient, but it also creates a much stronger shock profile across the upper surface of the wing. The remaining two cases mirrored the first two cases' angle of attack but decreased the freestream velocity to Mach 0.5; these cases showed stable attached flow with no formation of local shocks, illustrating the effect that transonic velocities have on a wing as the pressure disturbances would put stress on the wing's structure, requiring additional maintenance. When comparing our results for the transonic flow conditions with published data, there was a strong agreement between the two datasets that confirmed the validity and accuracy of our simulations. Were we to continue this project, we would have attempted to reconstruct the wing's drag polar and lift curve or investigated the effects of dihedral, sideslip, and other flow conditions on the wing's performance in flight.

References

[1] Gleize, V., Dumont, A., Mayeur, J., & Destarac, D. (2015). RANS simulations on TMR test cases and M6 wing with the Onera elsA flow solver (Invited). 53rd AIAA Aerospace Sciences Meeting. https://doi.org/10.2514/6.2015-1745

[2] Rumsey, C., “TURBULENCE MODEL NUMERICAL ANALYSIS 3D ONERA M6 Wing Validation Case,” Langley Research Center Turbulence Modeling Resource, Nov 10 2021. Retrieved 6 December 2024. https://turbmodels.larc.nasa.gov/onerawingnumerics_val.html